Journal of Computational Physics 229 (2010) 4097–4116

Contents lists available at ScienceDirect

Journal of Computational Physics

journal homepage: www.elsevier.com/locate/jcp

Large deformation of liquid capsules enclosed by thin shells immersed in the fluid

Duc-Vinh Le [a,*], Zhijun Tan [b]

[a] Institute of High Performance Computing, 1 Fusionopolis Way, #16-16 Connexis, Singapore 138632, Singapore
[b] Singapore-MIT Alliance, 4 Engineering Drive 3, National University of Singapore, Singapore 117576, Singapore

ARTICLE INFO

Article history:
Received 8 October 2009
Received in revised form 18 January 2010
Accepted 31 January 2010
Available online 12 February 2010

MSC:
65M06
76D05
74F10
92C10

Keywords:
Immersed boundary method
Navier–Stokes equations
Thin shell
Membrane capsules
Red-blood cells

ABSTRACT

The deformation of a liquid capsule enclosed by a thin shell in a simple shear flow is studied numerically using an implicit immersed boundary method. We present a thin-shell model for computing the forces acting on the shell middle surface during the deformation within the framework of the Kirchhoff–Love theory of thin shells. This thin-shell model takes full account of finite-deformation kinematics which allows thickness stretching as well as large deflections and bending strains. For hyperelastic materials, the plane-stress assumption is used to compute the hydrostatic pressure and the incompressibility condition yields the thickness strain component and the corresponding change in the thickness. The stresses developing over the cross-section of the shell are integrated over the thickness to yield the stress and moment resultants which are then used to compute the forces acting on the shell middle surface. The immersed boundary method is employed for calculating the hydrodynamics and fluid–structure interaction effects. The location of the thin shell is updated implicitly using the Newton–Krylov method. The present numerical technique has been validated by several examples including an inflation of a spherical shell and deformations of spherical and oblate spheroidal capsules in the shear flow.

1. Introduction

Many problems in which a viscous fluid interacts with a deformable boundary are of considerable interest in the study of fluid mechanics such as blood flow, suspension of liquid droplets in fluid. Understanding the mechanics of the interaction between the fluid and suspended particles is important in many applications such as chemical engineering, cellular biology and drug delivery. Much effort has been devoted to study the behavior of liquid capsules enclosed by elastic membrane such as red-blood cells and synthetic capsules with polymerized interfaces. Experimental and theoretical studies have revealed complex interaction of different physical properties of the capsule such as capsule shape, internal fluid viscosity and membrane material that affect the deformations of the suspended capsule in the flow.

Several experimental studies have been performed for synthetic capsules in simple shear flow [6,47,48]. Laboratory observations of red-blood cells (RBC) in the shear flow were also reported [1,15,35]. Depending on the shear rate and the stiffness of the membrane, the capsules or RBCs undergo different types of motion such as tank-treading, tumbling or transition from tumbling to tank-treading.

Theoretical study of the deformation of spherical capsules suspended in a shear flow was presented in [3,4] for small capsule deformation. For large deformation, asymptotic theories are not applicable and numerical simulations have been

* Corresponding author.
E-mail addresses: ledv@ihpc.a-star.edu.sg (D.-V. Le), smatz@nus.edu.sg (Z. Tan).

0021-9991/$ - see front matter © 2010 Elsevier Inc. All rights reserved.
doi:10.1016/j.jcp.2010.01.042

employed by a number of authors with different membrane models. In [10,13,24,43], the forces generated in the capsule membrane during the deformation are obtained using a finite element model [7,37]. Subsequently, a zero-thickness elastic shell model has been developed in [33] for computing the elastic tensions at the nodes of an unstructured quadratic triangular mesh describing the capsule membrane. This model was later used in [23,32] for studying capsule membrane with bending rigidity. Bending moments developed in [32] were expressed in terms of mean and Gaussian curvature multiplied by a corresponding bending modulus that is generally distinct from the modulus of elasticity. This constitutive law describes the mechanism that biological membranes consisting of lipid bilayers exhibit the bending moments due to a preferred three-dimensional unstressed configuration. These membrane models have been considered with different membrane constitutive laws. In most cases, the capsule membrane are considered as hyperelastic materials with neo-Hookean or Skalak strain energy functions [13,24,33,43]. The effect of the membrane constitutive laws on the deformation of capsules has been studied in [21]. Other forms of constitutive law have also been used such as the Yeoh form in [23] and the Hooke's law with 2d-Lamé coefficients in [18].

To handle the fluid–structure interaction, several methods have been employed to solve for the viscous incompressible fluid flow in conjunction with the membrane models. The boundary-element method (BEM) has been applied intensively to study the deformation of liquid capsules in Stokes flow [21,32,33]. A quadratic triangular mesh is used in [33] to discretize the membrane and the force is averaged over an element in the boundary integral. This method was plagued by numerical instabilities for high and low dimensionless shear rates due to the degradation of the grid. In [21], the boundary-element method is used in conjunction with surface interpolation by means of bi-cubic B-splines which allows accurate evaluation of high-order derivatives of the geometric quantities of the surface such as curvature. Recently, Kessler et al. [18] proposed a global spectral method in which the shape of the capsule is expanded into a set of smooth basis functions for Stokes flow. This method has the advantages that the resulting capsule shape is globally smooth and the derivatives of the basis functions are analytically known, which reduces the discretization error, especially in high-order derivatives such as the curvature. As an alternative to the boundary-element method, the immersed boundary (IB) method [30] has been employed to solve for the deformation of the elastic capsules in shear flow [13,24]. In addition, the immersed boundary method was also used with the lattice Boltzmann method (LBM) [43] to improve the efficiency by using multi-block-strategy. Recently, an implicit immersed boundary method has been proposed in [23] to improve the time step in advancing the location of the membrane with large elastic modulus. The implicit method has proven to be an efficient method in dealing with multiple liquid capsules in the flow.

In the present paper, we extent our implicit immersed boundary method [23] for simulating the deformation of liquid capsules immersed in the fluid. In [23], the zero-thickness shell model [33] was used for computing the forces generated on the membrane surface during deformation. As in [33], the implicit IB method also suffers from numerical instabilities for high and low deformations due to the grid degradation which leads to limit the extent of the simulation. In order to improve the simulation time, we employ the thin-shell model presented in [8,9] for computing stress and moment resultants. We note that in the present work, the liquid capsule is enclosed by a thin shell with finite thickness that exhibits bending resistance and the mechanism for generating the bending moments is different from that in [32]. Here, stresses developing over the cross-section of shells are integrated over the thickness to yield the stress resultants and tangential bending moments. In [8,9], the thin-shell model was proposed to compute the displacements of the shell nodal points on a subdivision surface with given loads. Here, we employed this thin-shell model to compute the stress and moment resultants with the known displacements on a quadratic triangular mesh. We also suggest a way to compute the total forces generated on each element and at each node of the mesh during the deformation.

Our goal in this work is twofold. First, we proposed a method for calculating the forces generated on the capsule surface by employing the thin-shell model [8,9] for studying non-linear deformation of liquid capsule enclosed by thin shell. Second, we investigate large deformations of capsules with various unstressed shapes. We also study different motions of non-spherical capsules such as tank-treading, tumbling and transition from tank-treading to tumbling under a broad range of dimensionless shear rate and viscosity ratio.

The remainder of this paper is organized as follow. In Section 2, we describe the governing equations for the fluid flow and introduce the shell kinematics relevant to large deformations. We begin with constitutive models and the weak form of static equilibrium equations for Kirchhoff–Love shell theory. In Section 3, we briefly summarize the immersed boundary algorithm, the spatial discretization of the thin shell and the method for advancing the membrane evolution in time. In Section 4, some numerical examples are presented to demonstrate the performance of the method and finally, some conclusions are given in Section 5.

2. Formulation

2.1. Governing equations

In a three-dimensional bounded fluid domain Ω_F that contains an enclosed thin shell $\Omega_S(t)$, we consider the incompressible Navier–Stokes equations formulated in primitive variables, written as

$$\rho(\boldsymbol{u}_t + (\boldsymbol{u}\cdot\nabla)\boldsymbol{u}) = -\nabla p + \nabla\cdot(\mu[\nabla\boldsymbol{u} + (\nabla\boldsymbol{u})^T]) + \boldsymbol{f}, \tag{1}$$

$$\nabla\cdot\boldsymbol{u} = 0, \tag{2}$$

where $\boldsymbol{u} = (u, v, w)^T$ is the fluid velocity, p is the pressure, ρ and μ are density and viscosity of the fluid, respectively. For simplicity, we assume that ρ is constant over the whole domain. The viscosity of the fluid can be written as

$$\mu(\boldsymbol{x}, t) = \mu_e[1 + (\lambda - 1)\Psi(\boldsymbol{x}, t)], \tag{3}$$

where μ_e is the viscosity of the external flow, λ is the ratio of the internal to the surrounding fluid viscosities, $\boldsymbol{x} = (x, y, z)$ is spatial position and $\Psi(\boldsymbol{x}, t)$ is an indicator function which is 1 in the interior of the shell and 0 outside.

The effect of the thin shell $\Omega_S(t)$ immersed in the fluid results in a singular force $\boldsymbol{f}$ which has the form

$$\boldsymbol{f}(\boldsymbol{x}, t) = \int_{\Omega_S(t)} \boldsymbol{F}^s(\xi^1, \xi^2, \xi^3, t)\delta(\boldsymbol{x} - \boldsymbol{X}(\xi^1, \xi^2, \xi^3, t))\mathrm{d}\Omega_S, \tag{4}$$

where (ξ^1, ξ^2, ξ^3) are curvilinear coordinates attached to the shell at a material point, $\boldsymbol{X}(\xi^1, \xi^2, \xi^3, t)$ is the position at time t in Cartesian coordinates of the material point whose label is (ξ^1, ξ^2, ξ^3) and $\boldsymbol{F}^s(\xi^1, \xi^2, \xi^3, t)$ is the force strength. Here, $\delta(\boldsymbol{x})$ is the three-dimensional Dirac function. The motion of the shell can be determined by integrating the equation

$$\frac{\mathrm{d}\boldsymbol{X}(\xi^1, \xi^2, \xi^3, t)}{\mathrm{d}t} = \int_{\Omega_F} \boldsymbol{u}(\boldsymbol{x}, t)\delta(\boldsymbol{x} - \boldsymbol{X}(\xi^1, \xi^2, \xi^3, t))\mathrm{d}\boldsymbol{x}. \tag{5}$$

2.2. Thin shell formulation

In this section we summarize the basic shell description and kinematic results underlying the shell model. Further details can be found in [8,9,38,39].

2.2.1. Kinematic description of the shell

In describing a shell, we follow Simo and Fox [38] and adopt the Kirchhoff–Love hypothesis, which requires that a fiber which is initially normal to the middle surface of the shell remains normal to the deformed middle surface of the shell. Consider a shell body whose undeformed and deformed middle surface are denoted by $\overline{\Gamma}$ and Γ, respectively. The position of a material point $\overline{\boldsymbol{X}}$ associated with the coordinates (ξ^1, ξ^2, ξ^3) within the shell in its undeformed configuration is given by

$$\overline{\boldsymbol{X}}(\xi^1, \xi^2, \xi^3) = \bar{\boldsymbol{\varphi}}(\xi^1, \xi^2) + \xi^3\bar{\boldsymbol{a}}_3(\xi^1, \xi^2), \tag{6}$$

where $\bar{\boldsymbol{\varphi}}(\xi^1, \xi^2)$ defines a parametric representation of the undeformed shell middle surface and $\bar{\boldsymbol{a}}_3(\xi^1, \xi^2)$ is the unit normal vector to the middle surface. The pair (ξ^1, ξ^2) is a system of surface curvilinear coordinates and ξ^3 is the thickness coordinate limited by $-\bar{h}/2 \leqslant \xi^3 \leqslant \bar{h}/2$, where $\bar{h}$ is the thickness of the undeformed shell. The position of a material point $\boldsymbol{X}$ associated with the coordinates (ξ^1, ξ^2, ξ^3) within the shell in its deformed configuration is given by

$$\boldsymbol{X}(\xi^1, \xi^2, \xi^3) = \boldsymbol{\varphi}(\xi^1, \xi^2) + \xi^3\eta(\xi^1, \xi^2)\boldsymbol{a}_3(\xi^1, \xi^2), \tag{7}$$

where $\boldsymbol{\varphi}$ and $\boldsymbol{a}_3$ define the deformed shell middle surface and its unit normal vector, respectively. The thickness stretch η is defined as

$$\eta = \frac{h_d}{\bar{h}}, \tag{8}$$

where h_d is the thickness of the deformed shell. The surface basis vectors corresponding to $\bar{\boldsymbol{\varphi}}$ and $\boldsymbol{\varphi}$ are

$$\bar{\boldsymbol{a}}_\alpha = \bar{\boldsymbol{\varphi}}_{,\alpha}, \quad \boldsymbol{a}_\alpha = \boldsymbol{\varphi}_{,\alpha}, \tag{9}$$

respectively, where here and henceforth a comma is used to denote partial differentiation and Greek indices take the values 1 and 2.

The unit normal vectors to the shell middle surfaces in the undeformed and deformed configurations are

$$\bar{\boldsymbol{a}}_3 = \frac{\bar{\boldsymbol{a}}_1 \times \bar{\boldsymbol{a}}_2}{|\bar{\boldsymbol{a}}_1 \times \bar{\boldsymbol{a}}_2|}, \quad \boldsymbol{a}_3 = \frac{\boldsymbol{a}_1 \times \boldsymbol{a}_2}{|\boldsymbol{a}_1 \times \boldsymbol{a}_2|}. \tag{10}$$

The local covariant basis vectors on the undeformed and deformed configurations are defined as

$$\bar{\boldsymbol{g}}_\alpha = \frac{\partial\overline{\boldsymbol{X}}}{\partial\xi^\alpha} = \bar{\boldsymbol{a}}_\alpha + \xi^3\bar{\boldsymbol{a}}_{3,\alpha}, \tag{11}$$

$$\bar{\boldsymbol{g}}_3 = \frac{\partial\overline{\boldsymbol{X}}}{\partial\xi^3} = \bar{\boldsymbol{a}}_3, \tag{12}$$

$$\boldsymbol{g}_\alpha = \frac{\partial\boldsymbol{X}}{\partial\xi^\alpha} = \boldsymbol{a}_\alpha + \xi^3(\eta\boldsymbol{a}_3)_{,\alpha}, \tag{13}$$

$$\boldsymbol{g}_3 = \frac{\partial\boldsymbol{X}}{\partial\xi^3} = \eta\boldsymbol{a}_3. \tag{14}$$

The corresponding covariant components of the metric tensors in both configurations are

$$\bar{g}_{ij} = \bar{\boldsymbol{g}}_i \cdot \bar{\boldsymbol{g}}_j, \quad g_{ij} = \boldsymbol{g}_i \cdot \boldsymbol{g}_j, \tag{15}$$

where here and henceforth lowercase Latin indices range from 1 to 3. Contravariant basis vectors $\bar{\boldsymbol{g}}^i$ and $\boldsymbol{g}^i$ are defined such that

$$\bar{\boldsymbol{g}}_i \cdot \bar{\boldsymbol{g}}^j = \delta_i^j, \quad \boldsymbol{g}_i \cdot \boldsymbol{g}^j = \delta_i^j, \tag{16}$$

where δ_i^j is the Kronecker delta. The corresponding contravariant metric tensors which will be required later are defined as

$$\bar{g}^{ij} = \bar{\boldsymbol{g}}^i \cdot \bar{\boldsymbol{g}}^j, \quad g^{ij} = \boldsymbol{g}^i \cdot \boldsymbol{g}^j. \tag{17}$$

In term of the co- and contravariant basis vectors, the deformation gradient tensor $\mathbf{F}$ for the shell body may be expressed in the form [25]

$$\mathbf{F} = \frac{\partial \boldsymbol{X}}{\partial \bar{\boldsymbol{X}}} = \frac{\partial \boldsymbol{X}}{\partial \xi^i} \otimes \bar{\boldsymbol{g}}^i = \boldsymbol{g}_i \otimes \bar{\boldsymbol{g}}^i, \tag{18}$$

where here and henceforth summation over the repeated index i is implied in the range from 1 to 3. Using the local covariant basis vectors expressed in Eqs. (13) and (14) the deformation gradient can be rewritten as

$$\mathbf{F} = \boldsymbol{a}_\alpha \otimes \bar{\boldsymbol{g}}^\alpha + \eta \boldsymbol{a}_3 \otimes \bar{\boldsymbol{g}}^3 + \xi^3 (\eta \boldsymbol{a}_3)_{,\alpha} \otimes \bar{\boldsymbol{g}}^\alpha, \tag{19}$$

where the derivative of the shell director can be computed from (10) as

$$\boldsymbol{a}_{3,\alpha} = \frac{(\boldsymbol{a}_{1,\alpha} \times \boldsymbol{a}_2 + \boldsymbol{a}_1 \times \boldsymbol{a}_{2,\alpha}) - \boldsymbol{a}_3[(\boldsymbol{a}_{1,\alpha} \times \boldsymbol{a}_2 + \boldsymbol{a}_1 \times \boldsymbol{a}_{2,\alpha}) \cdot \boldsymbol{a}_3]}{|\boldsymbol{a}_1 \times \boldsymbol{a}_2|}. \tag{20}$$

The right Cauchy–Green strain tensor is then given in terms of the deformation gradient tensor $\mathbf{F}$ as

$$\mathbf{C} = \mathbf{F}^{\mathrm{T}}\mathbf{F} = g_{ij} \bar{\boldsymbol{g}}^i \otimes \bar{\boldsymbol{g}}^j. \tag{21}$$

2.2.2. Constitutive models

To complete the mathematical formulation for the shell, we introduce constitutive equations that express the stress tensor in terms of the deformation tensors. We follow the procedure presented in [8] and consider the incompressible hyperelastic materials. For the incompressible hyperelastic material, such as Mooney elastic solids or biological membranes, we consider the Mooney–Rivlin strain energy function per unit undeformed volume

$$W(\mathbf{C}) = c_1(I_1^C - 3) + c_2(I_2^C - 3), \tag{22}$$

where c_1 and c_2 are material constants, and $I_1^C = \mathrm{tr}\mathbf{C}$ and $I_2^C = ((\mathrm{tr}\mathbf{C})^2 - \mathrm{tr}\mathbf{C}^2)/2$ are the first and second invariants of the right Cauchy–Green tensor $\mathbf{C}$, respectively. When $c_2 = 0$, the second term in (22) vanishes and Eq. (22) is known as neo-Hookean strain energy function,

$$W(\mathbf{C}) = \frac{E}{6}(I_1^C - 3), \tag{23}$$

where E is the Young's modulus.

The Kirchhoff stress tensor can be computed from the strain energy function as

$$\boldsymbol{\tau} = \mathbf{F} \cdot \frac{\partial W}{\partial \mathbf{C}} \cdot \mathbf{F}^T - p_s \mathbf{I}, \tag{24}$$

where p_s denotes the hydrostatic pressure and $\mathbf{I}$ is identity tensor. The Kirchhoff stress tensor can be expressed in an alternative form as

$$\boldsymbol{\tau} = \tau^{ij} \boldsymbol{g}_i \otimes \boldsymbol{g}_j \tag{25}$$

with the components τ^{ij} derived from the Doyle–Ericksen relation [25] as

$$\tau^{ij} = 2\frac{\partial W}{\partial g_{ij}} - p_s g^{ij}. \tag{26}$$

For Mooney–Rivlin hyperelastic materials the Kirchhoff stress components can be explicitly written as

$$\tau^{ij} = 2(c_1 + c_2 \bar{g}^{kl} g_{kl}) \bar{g}^{ij} - 2c_2 \bar{g}^{ik} g_{kl} \bar{g}^{lj} - p_s g^{ij}, \tag{27}$$

which is derived from the relations

$$\frac{\partial I_1^C}{\partial g_{ij}} = \bar{g}^{ij}, \tag{28}$$

$$\frac{\partial I_2^C}{\partial g_{ij}} = \bar{g}^{kl} g_{kl} \bar{g}^{ij} - \bar{g}^{ik} g_{kl} \bar{g}^{lj}. \tag{29}$$

Since this work deals with thin shells only, we may assume the plane stress state by requiring that

$$\tau^{33} = 2\frac{\partial W}{\partial g_{33}} = 0 \tag{30}$$

across the thickness of the shell [2,8,12]. The hydrostatic pressure p_s can be computed from the plane-stress assumption as

$$p_s = \frac{2(c_1 + c_2 \bar{g}^{kl} g_{kl}) \bar{g}^{33} - 2c_2 \bar{g}^{3k} g_{kl} \bar{g}^{l3}}{g^{33}}. \tag{31}$$

The thickness strain can be computed from the incompressibility condition

$$\det \mathbf{F} = \sqrt{\frac{\det(\boldsymbol{g})}{\det(\bar{\boldsymbol{g}})}} = 1 \tag{32}$$

with the result

$$g_{33} = \frac{\det(\bar{\boldsymbol{g}})}{g_{11} g_{22} - g_{12} g_{21}}. \tag{33}$$

Here, we have set $g_{\alpha 3}$ and $g_{3\alpha}$ to zero by virtue of the assumed shell kinematics. The thickness stretch is then evaluated as

$$\eta = \frac{1}{\bar{h}} \int_{-\bar{h}/2}^{\bar{h}/2} \sqrt{g_{33}} \mathrm{d}\xi^3. \tag{34}$$

To model for the red-blood cell (RBC) membrane, we can use the strain energy function proposed by Skalak et al. [40]

$$W = \frac{E}{4}\left(\frac{1}{2} I_1^2 + I_1 - I_2\right) + \frac{c_{11} E}{8} I_2^2, \tag{35}$$

where c_{11} is a large constant represents the ratio between the area dilation modulus and the shear modulus, and the invariants I_1 and I_2 are functions of the invariants I_1^C, I_2^C and g_{33} as

$$I_1 = I_1^C - 2 - g_{33}, \tag{36}$$

$$I_2 = I_2^C - 1 - (I_1^C - g_{33}) g_{33}. \tag{37}$$

2.2.3. Weak form of equilibrium

To derive the equilibrium equations of the shell body in weak form, we start from the fact that the potential energy of the shell body is stationary at equilibrium, i.e.

$$\delta \Pi = \delta \Pi_{\text{int}} + \delta \Pi_{\text{ext}} = 0, \tag{38}$$

where $\delta \Pi_{\text{ext}}$ is the variation of the potential energy of the external forces. The variation of the potential of the internal forces with an arbitrary variation $\delta \mathbf{F}$ can be expressed as

$$\delta \Pi_{\text{int}} = \int_{\overline{\Omega}_S} \frac{\partial W}{\partial \mathbf{F}} : \delta \mathbf{F} \mathrm{d}\overline{\Omega}_S = \int_{\overline{\Omega}_S} \mathbf{P} : \delta \mathbf{F} \mathrm{d}\overline{\Omega}_S, \tag{39}$$

where $\overline{\Omega}_S$ is the undeformed shell body and $\mathbf{P}$ is the first Piola–Kirchhoff stress tensor. Substitute Eq. (19) into (39) we have the expression for the internal virtual work

$$\delta \Pi_{\text{int}} = \int_{\overline{\Omega}_S} \mathbf{P} : [\delta \boldsymbol{a}_\alpha \otimes \bar{\boldsymbol{g}}^\alpha + \eta \delta \boldsymbol{a}_3 \otimes \bar{\boldsymbol{g}}^3 + \xi^3 (\eta \delta \boldsymbol{a}_3)_{,\alpha} \otimes \bar{\boldsymbol{g}}^\alpha] \mathrm{d}\overline{\Omega}_S + \int_{\overline{\Omega}_S} \mathbf{P} : [\delta \eta \boldsymbol{a}_3 \otimes \bar{\boldsymbol{g}}^3 + \xi^3 (\delta \eta \boldsymbol{a}_3)_{,\alpha} \otimes \bar{\boldsymbol{g}}^\alpha] \mathrm{d}\overline{\Omega}_S. \tag{40}$$

By recalling the relation $\mathbf{P} = \boldsymbol{\tau} \mathbf{F}^{-\mathrm{T}}$ and noting that $\boldsymbol{\tau} \cdot \boldsymbol{g}^i = \mathbf{P} \cdot \bar{\boldsymbol{g}}^i$ [38], the internal virtual work expression can be rewritten as

$$\delta \Pi_{\text{int}} = \int_{\overline{\Omega}_S} \boldsymbol{\tau} : [\delta \boldsymbol{a}_\alpha \otimes \boldsymbol{g}^\alpha + \eta \delta \boldsymbol{a}_3 \otimes \boldsymbol{g}^3 + \xi^3 (\eta \delta \boldsymbol{a}_3)_{,\alpha} \otimes \boldsymbol{g}^\alpha] \mathrm{d}\overline{\Omega}_S + \int_{\overline{\Omega}_S} \boldsymbol{\tau} : [\delta \eta \boldsymbol{a}_3 \otimes \boldsymbol{g}^3 + \xi^3 (\delta \eta \boldsymbol{a}_3)_{,\alpha} \otimes \boldsymbol{g}^\alpha] \mathrm{d}\overline{\Omega}_S. \tag{41}$$

Since the variations $\delta\boldsymbol{\varphi}$ and $\delta\eta$ are independent, Eq. (38) can be decoupled into the equations

$$\int_{\overline{\Gamma}}\int_{-\bar{h}/2}^{\bar{h}/2}\boldsymbol{\tau}:[\delta\boldsymbol{a}_\alpha\otimes\boldsymbol{g}^\alpha+\eta\delta\boldsymbol{a}_3\otimes\boldsymbol{g}^3+\xi^3(\eta\delta\boldsymbol{a}_3)_{,\alpha}\otimes\boldsymbol{g}^\alpha]\bar{v}\,\mathrm{d}\xi^3\,\mathrm{d}\overline{\Gamma}+\delta\Pi_{\mathrm{ext}}=0, \tag{42}$$

$$\int_{\overline{\Gamma}}\int_{-\bar{h}/2}^{\bar{h}/2}\boldsymbol{\tau}:[\delta\eta\boldsymbol{a}_3\otimes\boldsymbol{g}^3+\xi^3(\delta\eta\boldsymbol{a}_3)_{,\alpha}\otimes\boldsymbol{g}^\alpha]\bar{v}\,\mathrm{d}\xi^3\,\mathrm{d}\overline{\Gamma}=0, \tag{43}$$

where

$$\bar{v}=\frac{|(\bar{\boldsymbol{g}}_1\times\bar{\boldsymbol{g}}_2)\cdot\bar{\boldsymbol{g}}_3|}{|(\bar{\boldsymbol{a}}_1\times\bar{\boldsymbol{a}}_2)\cdot\bar{\boldsymbol{a}}_3|} \tag{44}$$

accounts for the curvature of the shell in the volume integration. Eq. (42) is the balance equation of the middle surface of the shell, whereas Eq. (43) establishes the equilibrium across the shell thickness. The equilibrium across the shell thickness can be alternatively enforced by using the plane-stress assumption [8]. Following [8,38], we define the stress resultant $\boldsymbol{n}^\alpha$, and the moment resultant $\boldsymbol{m}^\alpha$ as

$$\boldsymbol{n}^\alpha=\int_{-\bar{h}/2}^{\bar{h}/2}\boldsymbol{\tau}\cdot\boldsymbol{g}^\alpha\bar{v}\,\mathrm{d}\xi^3, \tag{45}$$

$$\boldsymbol{m}^\alpha=\int_{-\bar{h}/2}^{\bar{h}/2}\boldsymbol{\tau}\cdot\boldsymbol{g}^\alpha\xi^3\bar{v}\,\mathrm{d}\xi^3. \tag{46}$$

In addition, one defines the across-the-thickness stress resultant, denoted by $\boldsymbol{l}$, by the expression

$$\boldsymbol{l}=\int_{-\bar{h}/2}^{\bar{h}/2}\boldsymbol{\tau}\cdot\boldsymbol{g}^3\bar{v}\,\mathrm{d}\xi^3. \tag{47}$$

Then Eq. (42) can be simplified as

$$\int_{\overline{\Gamma}}[\boldsymbol{n}^\alpha\cdot\delta\boldsymbol{a}_\alpha+\eta\boldsymbol{l}\cdot\delta\boldsymbol{a}_3+\boldsymbol{m}^\alpha\cdot(\eta\delta\boldsymbol{a}_3)_{,\alpha}]\mathrm{d}\overline{\Gamma}+\delta\Pi_{\mathrm{ext}}=0. \tag{48}$$

3. Numerical methods

3.1. Description of the IB and projection methods

The immersed boundary method uses a set of NP control points $\mathbf{x}_l,\ l=1,\ldots,\mathrm{NP}$ to represent the middle surface of the thin shell. The force density is computed at these control points and is distributed to the Cartesian grid points using a discrete representation of the delta function,

$$\boldsymbol{f}(\boldsymbol{x},t)=\sum_{l=1}^{\mathrm{NP}}\boldsymbol{f}_l^s(\xi^1,\xi^2,t)D_h(\boldsymbol{x}-\mathbf{x}_l(t))\Delta\xi^1\Delta\xi^2, \tag{49}$$

where $\boldsymbol{f}_l^s(\xi^1,\xi^2,t)$ is the force per unit area at the control point $\mathbf{x}_l$ whose label is (ξ^1,ξ^2). $D_h(\boldsymbol{x})$ is a three-dimensional discrete delta function,

$$D_h(\boldsymbol{x})=\frac{1}{h^3}\vartheta\left(\frac{x}{h}\right)\vartheta\left(\frac{y}{h}\right)\vartheta\left(\frac{z}{h}\right), \tag{50}$$

where h is the grid size, x, y and z are the Cartesian components of $\boldsymbol{x}$ and ϑ is a continuous function which is taken from [34] and given by

$$\vartheta(d)=\begin{cases}\frac{1}{6}(5-3|d|-\sqrt{1-3(1-|d|)^2}), & 0.5\leqslant|d|\leqslant1.5,\\ \frac{1}{3}(1+\sqrt{-3d^2+1}), & |d|\leqslant0.5,\\ 0, & \text{otherwise.}\end{cases} \tag{51}$$

Once the force density is computed at the control points and distributed to the grid, the Navier–Stokes equations with the forcing terms are then solved for the pressure and velocity field at the Cartesian grid points using the projection method [5]. Our numerical algorithm is based on the pressure increment projection algorithm for the discretization of the Navier–Stokes equations. The spatial discretization is carried out on a standard marker-and-cell (MAC) staggered grid similar to that described in Kim and Moin [19]. Given the velocity $\boldsymbol{u}^n$, the pressure $p^{n-1/2}$ and the forcing term $\boldsymbol{f}^{n+1/2}$, we compute the intermediate velocity $\boldsymbol{u}^*$ by solving

$$\rho\frac{\boldsymbol{u}^*-\boldsymbol{u}^n}{\Delta t}=-\rho(\boldsymbol{u}\cdot\nabla\boldsymbol{u})^{n+\frac{1}{2}}-G^{MAC}p^{n-\frac{1}{2}}+\nabla\cdot(\mu[\nabla\boldsymbol{u}^*+(\nabla\boldsymbol{u}^n)^T])+\boldsymbol{f}^{n+\frac{1}{2}}, \tag{52}$$

where the advective term is extrapolated using the formula,

$$(\boldsymbol{u}\cdot\nabla\boldsymbol{u})^{n+\frac{1}{2}} = \frac{3}{2}(\boldsymbol{u}\cdot\nabla_h\boldsymbol{u})^{n} - \frac{1}{2}(\boldsymbol{u}\cdot\nabla_h\boldsymbol{u})^{n-1}. \tag{53}$$

We then compute a pressure increment ϕ^{n+1} and update the pressure and velocity field as

$$\nabla_h^2\phi^{n+1} = \rho\frac{D^{MAC}\boldsymbol{u}^*}{\Delta t}, \tag{54}$$

$$\boldsymbol{u}^{n+1} = \boldsymbol{u}^* - \frac{1}{\rho}\Delta t G^{MAC}\phi^{n+1}, \tag{55}$$

$$p^{n+1/2} = p^{n-1/2} + \phi^{n+1}. \tag{56}$$

In the above expressions, ∇_h and ∇_h^2 are the standard central difference operators, G^{MAC} and D^{MAC} are the MAC gradient and divergence operators, respectively [22]. The velocity field is then interpolated to find the velocity at the control points as,

$$\boldsymbol{u}(\mathbf{x}_I,t) = \sum_{\boldsymbol{x}}\boldsymbol{u}(\boldsymbol{x},t)D_h(\boldsymbol{x}-\mathbf{x}_I(t))h^3, \tag{57}$$

and this velocity is used to advance the position of the immersed boundary. As the immersed boundary moves and deforms, the entire fluid viscosity can be updated everywhere by solving the Poisson equation for the indicator function $\Psi(\boldsymbol{x},t)$ [45,46] as

$$\nabla^2\Psi = \nabla\cdot\boldsymbol{G}, \tag{58}$$

where $\boldsymbol{G}$ is the gradient of the indicator function defined as

$$\boldsymbol{G}(\boldsymbol{x}) = \int_\Gamma \boldsymbol{a}_3\delta(\boldsymbol{x}-\varphi(\xi^1,\xi^2))\mathrm{d}\Gamma. \tag{59}$$

In the numerical implementation of the projection method, we used the alternating direction implicit (ADI) method [11,17] to solve Eq. (52) for the intermediate velocity. Eqs. (54) and (58) are solved using a Fast Fourier Transform algorithm [36].

3.2. Spatial discretization of the thin shell

Next we proceed to discretize the middle surface of the shell into an unstructured mesh of triangular elements. This mesh may be taken as a basis for introducing an interpolation of the general form

$$\mathbf{x}(\xi^1,\xi^2) = \sum_{I=1}^{\mathrm{NP}} N^I(\xi^1,\xi^2)\mathbf{x}_I \tag{60}$$

for the deformed middle surface of the shell. In (60) $\{N^I,\ I=1,\ldots,\mathrm{NP}\}$ are the shape functions, $\{\mathbf{x}_I,\ I=1,\ldots,\mathrm{NP}\}$ are the corresponding nodal coordinates, and NP is the total number of nodes in the mesh. Introducing the interpolated parametric equation (60) into the weak form (48), we have

$$\int_{\overline{\Gamma}}\left[\boldsymbol{n}^\alpha\cdot\frac{\partial\boldsymbol{a}_\alpha}{\partial\mathbf{x}_I} + \eta\boldsymbol{l}\cdot\frac{\partial\boldsymbol{a}_3}{\partial\mathbf{x}_I} + \boldsymbol{m}^\alpha\cdot\left(\eta\frac{\partial\boldsymbol{a}_3}{\partial\mathbf{x}_I}\right)_{,\alpha}\right]\mathrm{d}\overline{\Gamma} + \int_\Gamma \boldsymbol{f}^s N^I\,\mathrm{d}\Gamma = 0 \tag{61}$$

for $I=1,\ldots,\mathrm{NP}$. The forces at node I can be approximated by averaging as

$$\boldsymbol{f}_I^s = \frac{\int_\Gamma \boldsymbol{f}^s N^I\,\mathrm{d}\Gamma}{\int_\Gamma N^I\,\mathrm{d}\Gamma}. \tag{62}$$

Introduction of (61) into (62) leads to the expression

$$\boldsymbol{f}_I^s = -\frac{\boldsymbol{f}_I^{\mathrm{int}}}{\int_\Gamma N^I\,\mathrm{d}\Gamma}, \tag{63}$$

where $\boldsymbol{f}_I^{\mathrm{int}}$ is the internal force at node I and follows in the form

$$\boldsymbol{f}_I^{\mathrm{int}} = \int_{\overline{\Gamma}}\left[\boldsymbol{n}^\alpha\cdot\frac{\partial\boldsymbol{a}_\alpha}{\partial\mathbf{x}_I} + \eta\boldsymbol{l}\cdot\frac{\partial\boldsymbol{a}_3}{\partial\mathbf{x}_I} + \boldsymbol{m}^\alpha\cdot\left(\eta\frac{\partial\boldsymbol{a}_3}{\partial\mathbf{x}_I}\right)_{,\alpha}\right]\mathrm{d}\overline{\Gamma}. \tag{64}$$

The internal force at node I is the sum of element contributions as in the standard finite element method. The contribution to the internal force at node I from a generic element is

$$\boldsymbol{f}_I^{\mathrm{int}} = \sum_k\left[\left(\boldsymbol{n}^\alpha\cdot\frac{\partial\boldsymbol{a}_\alpha}{\partial\mathbf{x}_I} + \eta\boldsymbol{l}\cdot\frac{\partial\boldsymbol{a}_3}{\partial\mathbf{x}_I} + \boldsymbol{m}^\alpha\cdot\left(\eta\frac{\partial\boldsymbol{a}_3}{\partial\mathbf{x}_I}\right)_{,\alpha}\right)\bar{j}\right]_{(\xi_k^1,\xi_k^2)} w_k, \tag{65}$$

where $\bar{j} = |\bar{\boldsymbol{a}}_1 \times \bar{\boldsymbol{a}}_2|$, (ξ_k^1, ξ_k^2) and w_k are the coordinate and weight of the kth Gaussian quadrature point, respectively. The stress and moment resultants at a Gaussian quadrature point are computed by numerical integration of the stresses across the thickness of the shell using the three-point Simpson rule.

In the present work, the geometry of each element is prescribed parametrically using six nodes, three located at the vertices and three along the edges, and the basis functions are quadratic functions given by Pozrikidis [31]. With these basic functions, both the numerator and denominator of the right-hand side in (63) are very small at the vertices of the element. And this may affect the accuracy of the forces $\boldsymbol{f}_I^s$ at the vertices. To avoid such a small denominator, one can use other basis functions such as the box-spline basis functions [42] as using in [8,9] for thin-shell model with subdivision surfaces. In the present context, we compute the total force $\boldsymbol{f}_{E_n}^s$ on an element E_n with area S_n as

$$\boldsymbol{f}_{E_n}^s = -\sum_{I=1}^{6} \frac{\boldsymbol{f}_I^{\text{int}} S_n}{S_I}, \tag{66}$$

where S_I is the total area of the elements that contain the local node I. And the force $\boldsymbol{f}_I^s$ at the node are the sum of the total force on the elements sharing the node, weighted by the angles formed by the element edges.

3.3. Advancing the membrane

The position of the immersed boundary, $\mathbf{x}_I$, is advanced in time in an implicit manner as

$$\mathbf{x}_I^{n+1} = \mathbf{x}_I^n + \Delta t(\boldsymbol{u}^{n+1/2}(\mathbf{x}_I^{n+1/2})), \tag{67}$$

where $\boldsymbol{u}^{n+1/2} = (\boldsymbol{u}^n + \boldsymbol{u}^{n+1})/2$ and $\mathbf{x}_I^{n+1/2} = (\mathbf{x}_I^n + \mathbf{x}_I^{n+1})/2$. Eq. (67) is implicit and couples the motion of the membrane with the solution at all grid points. Therefore at each time step, we need to solve a non-linear system of equations for the position of the control points of the form

$$\boldsymbol{g}(\mathbf{x}_I^{n+1}) = \mathbf{0}, \tag{68}$$

where

$$\mathbf{g}(\mathbf{x}_I) = \mathbf{x}_I - \mathbf{x}_I^n - \Delta t\left(\boldsymbol{u}^{n+1/2}\left(\frac{\mathbf{x}_I^n + \mathbf{x}_I}{2}\right)\right). \tag{69}$$

This non-linear system of equations is solved by a Jacobian-free Newton–Krylov (JFNK) method [20,23]. More details on the Jacobian-free Newton–Krylov can be found in [20] and the references therein.

In summary, given the location of the control points $\mathbf{x}_I^n$, the velocity field $\boldsymbol{u}^n$, the pressure field $p^{n-1/2}$ and the viscosity μ^n, the process of computing the new velocity $\boldsymbol{u}^{n+1}$, pressure field $p^{n+1/2}$, the viscosity μ^{n+1} and the location of the control points $\mathbf{x}_I^{n+1}$ can be summarized as follows:

Step 1: Set $k := 0$ and make an initial guess for $\mathbf{x}_I^{n+1}$, i.e. $\mathbf{x}_I^{(0)}$ as

$$\mathbf{x}_I^{(0)} = 2\mathbf{x}_I^n - \mathbf{x}_I^{n-1}.$$

Step 2:

- Solve Eq. (58) and update the viscosity μ^{n+1}.
- Evaluate the forces with the shell location $\mathbf{x}_I^{n+1/2} = (\mathbf{x}_I^n + \mathbf{x}_I^{(k)})/2$ as described in Section 3.2.

Step 3:

- Distribute the forces to the nearby Cartesian grid points using (49).
- Solve the Navier–Stokes equations using the projection method as described in Section 3.1.
- Compute the velocity at the control points, $\boldsymbol{u}^{n+1}(\mathbf{x}_I^{(k)})$ by interpolating from the velocity at the surrounding grid points using (57).

Step 4:

- Evaluate

$$\boldsymbol{g}(\mathbf{x}_I^{(k)}) = \mathbf{x}_I^{(k)} - \mathbf{x}_I^n - \Delta t\left(\boldsymbol{u}^{n+1/2}\left(\frac{\mathbf{x}_I^n + \mathbf{x}_I^{(k)}}{2}\right)\right).$$

- If $\|\boldsymbol{g}^{(k)}\| < \epsilon$ then $\mathbf{x}_I^{n+1} = \mathbf{x}_I^{(k)}$ and stop the iteration. Otherwise, update $\mathbf{x}_I^{(k+1)}$ using GMRES method. Set $k := k + 1$ and go to step 2.

4. Numerical results

4.1. Inflation of a sphere

This example considers the inflation of a spherical incompressible shell loaded by an internal pressure p. The problem of the inflation of a sphere tests the accuracy and convergence properties of the thin-shell model under conditions of large membrane deformations. The spherical shell is subjected to a prescribed increase in radius. A closed-form analytical solution [8,16,27,29] for the internal pressure at equilibrium is given as

$$p = \frac{\bar{h}}{\bar{R}\gamma^2}\frac{dW}{d\gamma}, \tag{70}$$

where $\gamma = R/\bar{R}$ is the radial stretch ratio, $\bar{R}$ and R are the radius of the undeformed and deformed middle surfaces of the shell, respectively and W is the strain energy function. For the Mooney–Rivlin material with the strain energy function (22), the relation between the radial stretch ratio γ and the internal pressure p follows from (70) as

$$p = \frac{4\bar{h}}{\bar{R}\gamma^7}(\gamma^6 - 1)(c_1 + c_2\gamma^2), \tag{71}$$

where c_1 and c_2 are the material constants. We performed simulations for the shell with undeformed radius $\bar{R} = 1$ and thickness $\bar{h} = 0.02$. The Mooney–Rivlin material constants c_1, c_2 are set to 20 and 10, respectively. We vary the radial stretch ratio γ from 1 to 5 and compute the average pressure loads on the shell. Calculations are performed with three meshes containing 128, 512 and 2048 elements, respectively. Fig. 1 shows the exact solution and the three numerical solutions. Good agreement between exact and numerical solutions and the general trend towards convergence can be observed in this figure.

4.2. Thin-shell capsule in simple shear flow

The present method is used to study the deformation of capsules enclosed by thin shells with spherical, spheroidal and biconcave unstressed shapes in simple shear flow given by the velocity $\boldsymbol{u} = (\dot{\gamma}z, 0, 0)$, where $\dot{\gamma}$ is the shear rate. Simulations are performed over a wide range of dimensionless shear rate and for a broad range of the ratio of the internal to surrounding fluid viscosities. For a capsule of volume V, the dimensionless shear rate which expresses the ratio of external viscous stresses to restoring elastic tensions is defined as

$$G = \frac{\mu_e \dot{\gamma} a}{E\bar{h}}, \tag{72}$$

where a is the radius of an isovolumic sphere, $a = (3V/4\pi)^{1/3}$. The Reynolds number is defined as

$$Re = \frac{\rho\dot{\gamma}a^2}{\mu_e}, \tag{73}$$

where ρ is the density of the fluid. The radius a is chosen to be sufficiently small so that the Reynolds number of the flow is effectively zero; in this work, it is set at $Re = 0.01$ unless stated otherwise. Hence, the inertia effect is negligible and the results can be compared with those obtained by the linear theory [4] or the BEM [32,33]. The center of the capsule is placed at

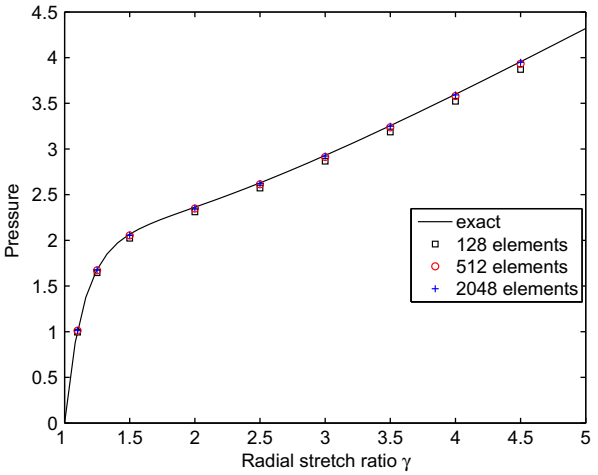

Fig. 1. Inflation of a Mooney–Rivlin sphere.

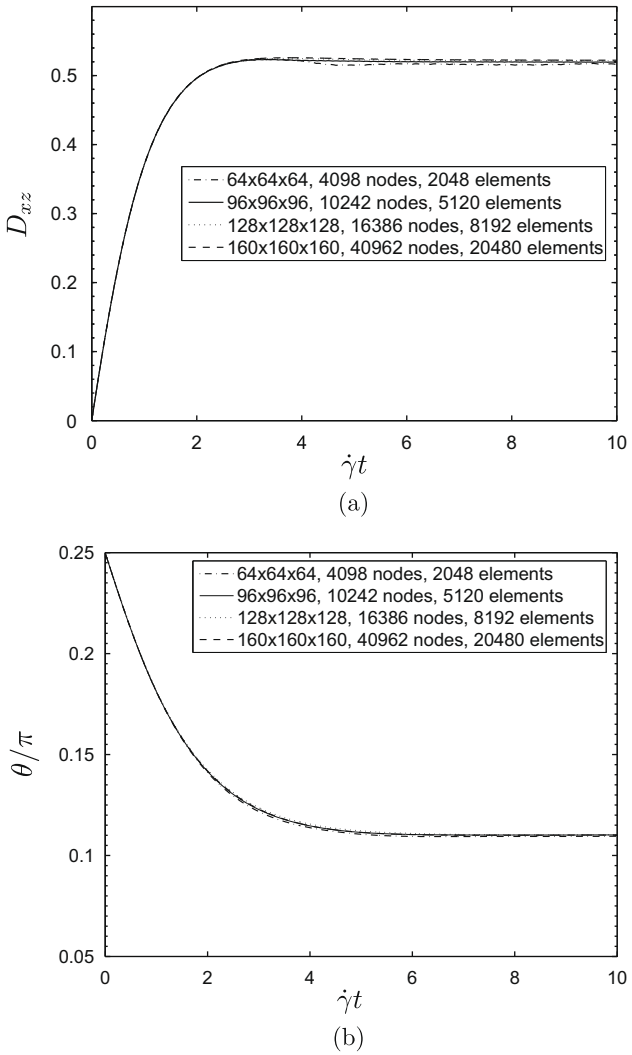

Fig. 2. Grid refinement study of (a) the deformation parameter and (b) inclination angle for spherical capsule with $\lambda = 1$ and $G = 0.2$.

the center of a cube of side $10a$. This computational domain is large enough so that boundary effects are not important [24,43]. Boundary conditions for the velocity are of the Dirichlet type at $z = \pm 5a$ and periodic at other boundaries. In the subsequent simulations, the initial capsule shape is taken to be a strain free state and the undeformed thickness of the enclosed shell is chosen to be $0.02a$.

4.2.1. Spherical capsules

In this example, we study the deformation of a spherical neo-Hookean thin shell in the shear flow. To validate the present method, we perform grid convergence study and compare the results with the linear theory [4] and those obtained numerically [21,33,43]. The deformation of the membrane is described by the Taylor shape parameter $D_{xz} = (L - B)/(L + B)$, where L and B are the maximum and minimum radial distances from the origin in the plane of shear, respectively. In practice, we find it more suitable to use the deformation parameter of an ellipsoid with the same inertia tensor as described in [24,33]. Grid refinement study is carried out for $G = 0.2$ and $\lambda = 1$. We started the grid refinement study with a $64 \times 64 \times 64$ fluid grid and a coarse shell surface discretization with a quadratic triangular mesh of 4098 nodes and 2048 elements. We then use $96 \times 96 \times 96$ and $128 \times 128 \times 128$ fluid grids with finer shell surface meshes of 10242 nodes, 5120 elements and 16,386 nodes, 8192 elements, respectively. Finally, the simulation is performed on the $160 \times 160 \times 160$ fluid grid with the finest surface mesh of 40,962 nodes and 20,480 elements. The results for the deformation parameter, D_{xz}, and inclination angle, θ, at different grid resolutions are shown in Fig. 2. The results show that the solutions converge with increasing grid resolution and the $96 \times 96 \times 96$ fluid grid and the surface mesh of 10,242 nodes and 5120 elements is sufficient to capture accurately the deformation parameters of the capsule. This fluid grid and surface mesh are used in the subsequent simulations unless stated otherwise.

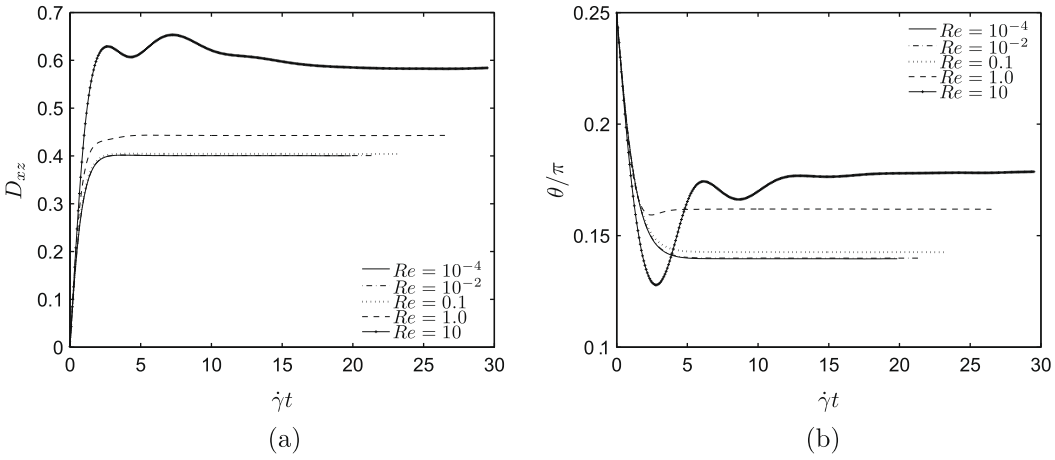

Fig. 3. The time evolutions of (a) the deformation parameter and (b) inclination angle for spherical capsule with $\lambda = 1$ and $G = 0.1$ at a sequence of Reynolds numbers.

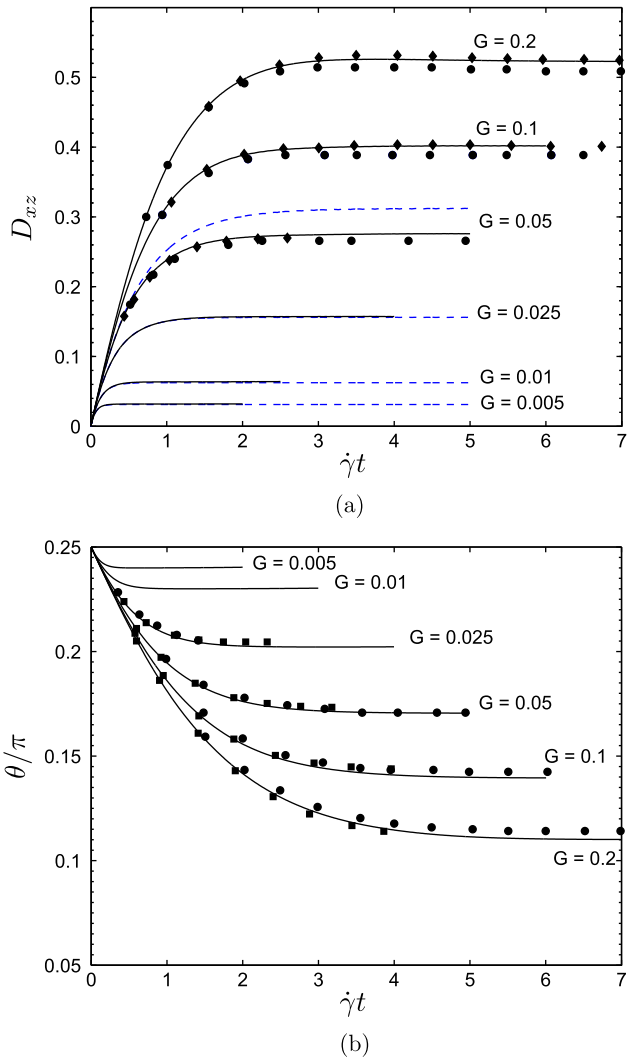

Fig. 4. The time evolutions of (a) the deformation parameter and (b) inclination angle for spherical capsule with $\lambda = 1$ at a sequence of dimensionless shear rates G. The solid lines are the results obtained by the present algorithm, the dashed lines are obtained with the linear theory. The circles and diamonds are found using the BEM [33,21] and the squares are obtained using IB-LBM [43].

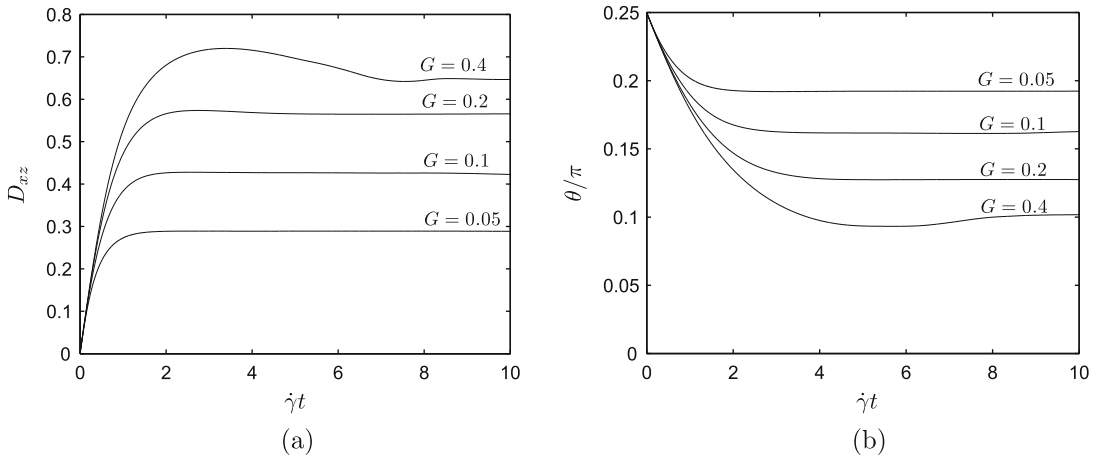

Fig. 5. The time evolutions of (a) the deformation parameter and (b) inclination angle for spherical capsule with $\lambda = 0.2$ at a sequence of dimensionless shear rates G.

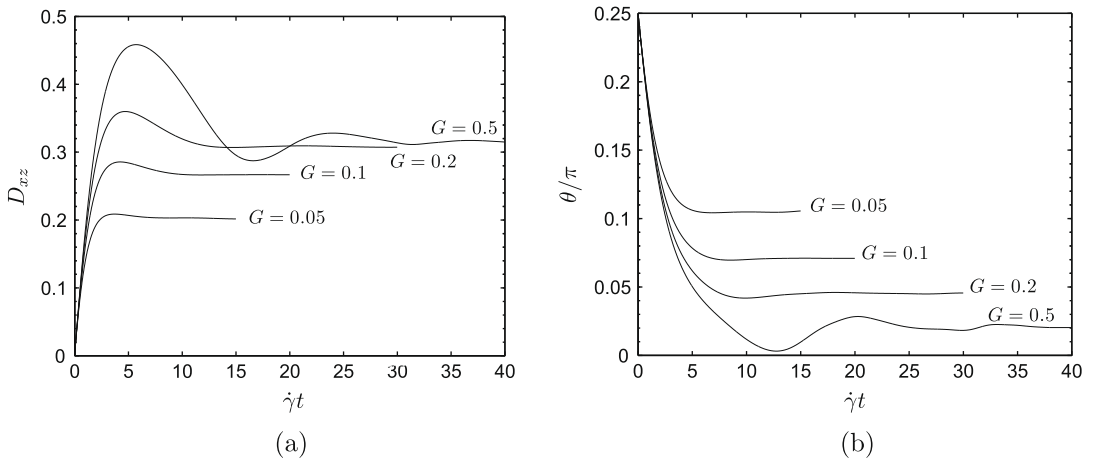

Fig. 6. The time evolutions of (a) the deformation parameter and (b) inclination angle for spherical capsule with $\lambda = 5$ at a sequence of dimensionless shear rates G.

Next, we study the inertia effect on the capsule deformation by varying Reynolds number from 10^{-4} to 10. It can be seen from Fig. 3 that increasing Reynolds number leads to greater deformation and decreased alignment with the undisturbed flow. At $Re \leqslant 0.1$, the deformation curves are almost identical which suggests that the inertia effect can be negligible. At moderate Reynolds number, $Re = 10$, the capsule oscillates before reaching a steady state. Similar transient process was observed for elastic capsule in [43].

Next, we study the deformation of spherical capsules over a range of dimensionless shear rate G and viscosity ratio λ. The time evolutions of the Taylor shape parameter, D_{xz}, and the inclination angle, θ, with several values of the dimensionless parameter G at $\lambda = 1$ are shown in Fig. 4. There is excellent agreement with the linear theory [4] at small G ($G < 0.025$) since the deformations are small. As the value of G increases the deformations increase and the linear theory does not apply. For larger values of G, we compare our results with those obtained using the BEM [21,33] and the immersed boundary lattice Boltzmann method (IB-LBM) [43] and Fig. 4 shows good agreement between the present method and other numerical methods. Figs. 5 and 6 show the deformation parameter, D_{xz}, and the inclination angle, θ, at $\lambda = 0.2$ and $\lambda = 5$, respectively. In both cases, the initial spherical capsules deform to nearly ellipsoidal steady shapes which are inclined with respect to the x-axis at well-defined angles, and the capsule membranes rotate around the interior fluid in a tank-treading mode [33]. As can be seen from Figs. 4–6, the capsules elongate and tend to align with the streamlines of the unperturbed flow when the value of G is increased at constant λ. And as λ increases at constant G, it leads to greater alignment of the capsule with the undisturbed flow. We note that the capsule volume change is within 0.3% during the simulations for all the values of G and λ.

Finally, we study the deformation of spherical capsules with Skalak's strain energy function (35). Simulations are carried out for three values of the ratio between the area dilation modulus and the shear elastic modulus, $c_{11} = 1, 10, 50$ at different

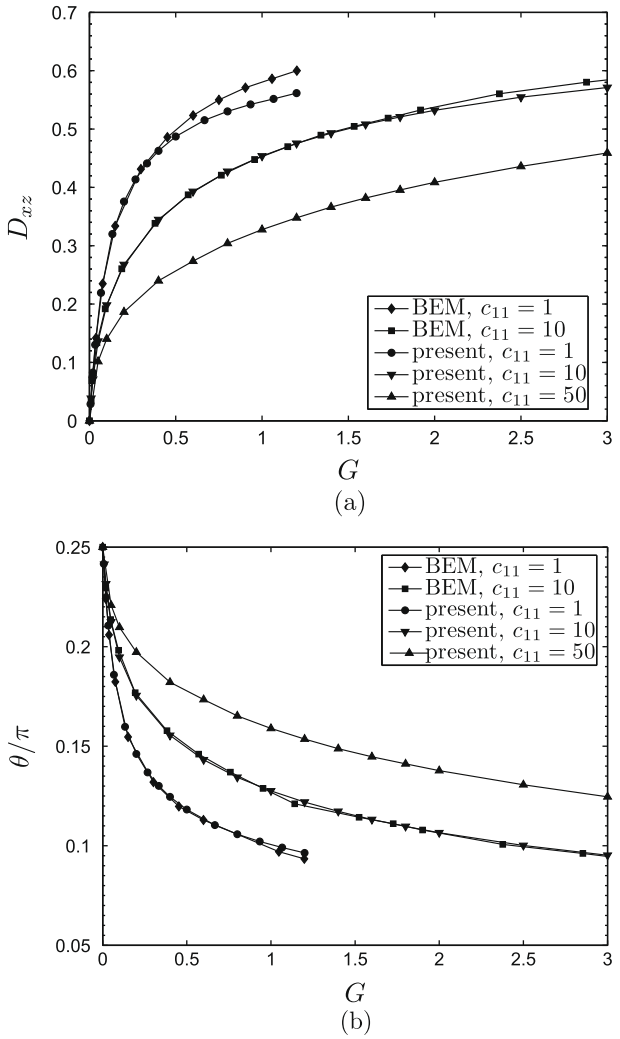

Fig. 7. (a) The deformation parameter and (b) inclination angle for spherical capsule governed by Skalak strain energy function (35) with the three values of c_{11} at $\lambda = 1$. The results are compared with those obtained using the BEM [21].

dimensionless shear rates G. Similar to the neo-Hookean membrane, the capsule deforms to a steady state and the membrane rotates around the interior fluid in a tank-treading mode. In Fig. 7, we plot the deformation parameter, D_{xz}, and the inclination angle, θ at steady state against the dimensionless shear rate G. The results are compared with those obtained using the BEM [21] and satisfactory agreements are observed in Fig. 7.

4.2.2. Oblate spherical capsules

In the preceding section, spherical capsules have been considered because of their ideal geometry which allows analytical methods to predict deformations histories. In practice, liquid capsules deviate from perfect spheres and may have a biconcave disk shape. Here, we simulate capsules whose initial shapes are oblate spheroids with different aspect ratios and biconcave disks. To describe an oblate spheroid with aspect ratio of b/a, we use the mapping $x_{obl} = Rx,\ y_{obl} = Ry,\ z_{obl} = (b/a)Rz$ where (x,y,z) is the coordinate of a point on the unit sphere and the radius R is adjusted to preserve the volume. Similarly, to describe the biconcave disk shape assumed by red-blood cells at rest, we use the mapping [14]

$$\begin{aligned} x_{rbc} &= Rx, \quad y_{rbc} = Ry, \\ z_{rbc} &= \pm 0.5R\sqrt{1-r^2}(C_0 + C_1 r^2 + C_2 r^4), \end{aligned} \tag{74}$$

where $r^2 = x^2 + y^2 \leqslant 1,\ C_0 = 0.2072,\ C_1 = 2.0026$, and $C_2 = -1.1228$. Once again, the strain energy function for the neo-Hookean material is employed.

First, we consider an oblate spheroid of aspect ratio $b/a = 0.9$, inclined at the angle $\theta_0 = \pi/4$ with respect to the streamlines of the unperturbed flow. These parameters were chosen to compare the evolution of the deformation parameter with

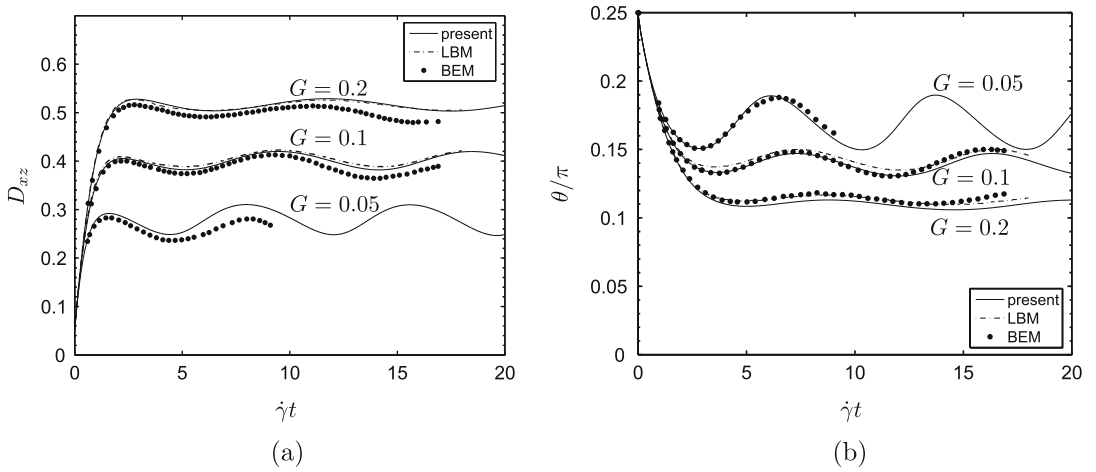

Fig. 8. Comparison of (a) the deformation parameter and (b) the inclination angle for oblate spheroidal capsules with $b/a = 0.9$ and $\lambda = 1$ at different dimensionless shear rates G with those obtained by the BEM [33] and LBM [43].

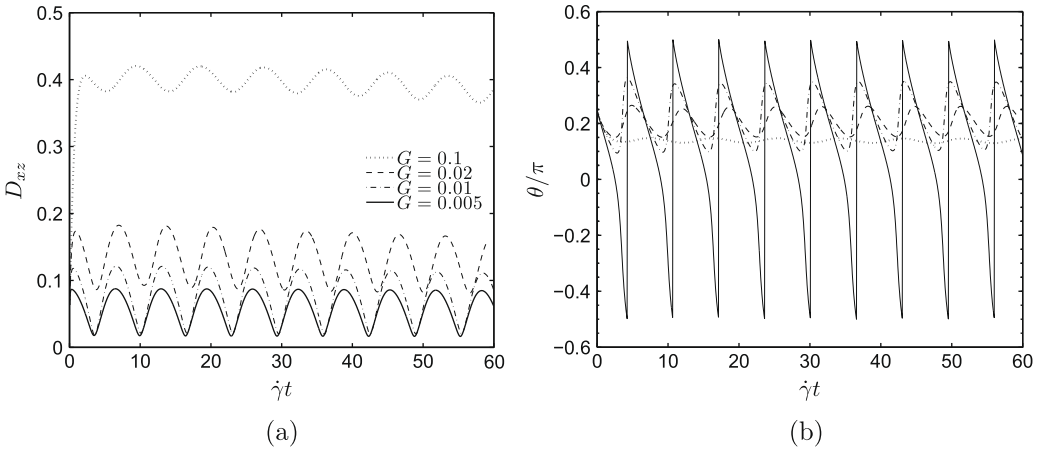

Fig. 9. The time evolutions of (a) the deformation parameter and (b) inclination angle for oblate spheroidal capsules with $b/a = 0.9$ and $\lambda = 1$ at different dimensionless shear rates G.

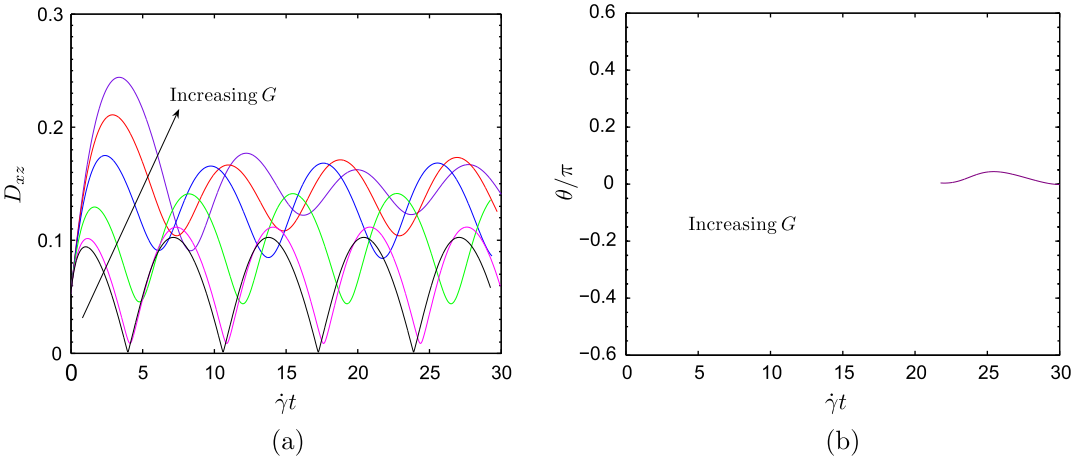

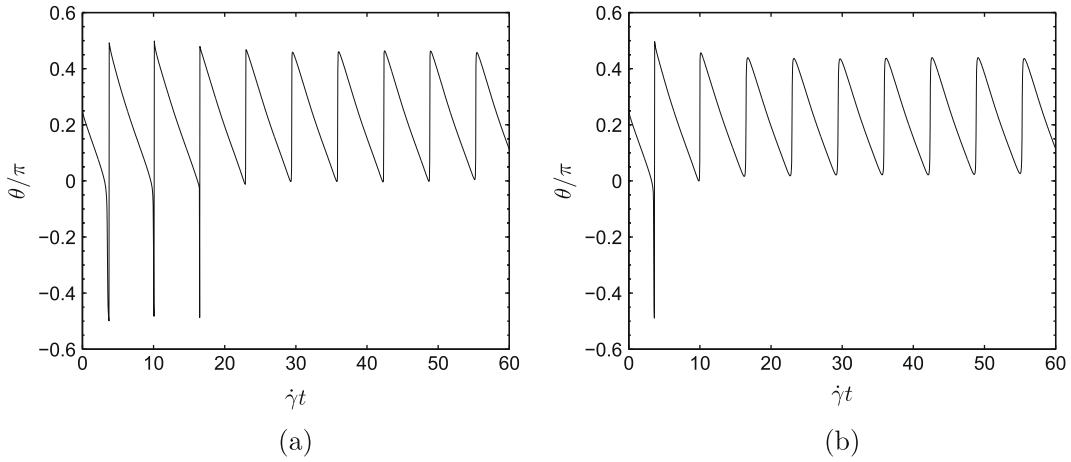

Fig. 11. The time evolutions of the inclination angle for oblate spheroidal capsules with $b/a = 0.9$ and $\lambda = 1$ at (a) $G = 0.0072$ and (b) $G = 0.0074$.

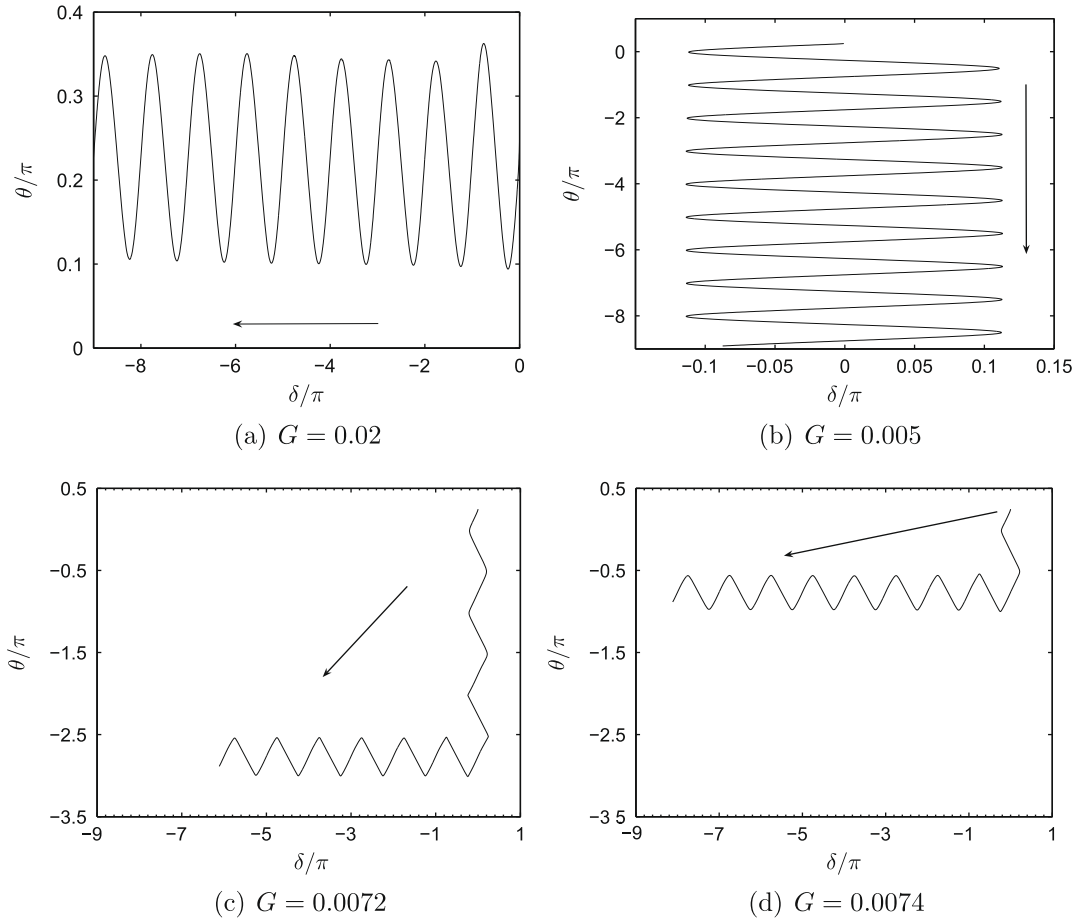

Fig. 12. Typical plots of inclination angle θ vs. phase angle δ for oblate spheroidal capsules with $b/a = 0.9$ and $\lambda = 1$. (a) typical tank-treading motion; (b) typical tumbling motion; (c,d) typical motions for tumbling to swinging transition.

those calculate using the BEM [33] and the lattice Boltzmann method (LBM) [43] under the same conditions. The deformation parameter D_{xz} and the inclination angle θ are calculated for three shear rates $G = 0.05, 0.1$ and 0.2 at $\lambda = 1$ and are shown in Fig. 8 as solid lines. Unlike the spherical capsule, the oblate spheroid capsule undergoes oscillations in the deformation parameter and the inclination angle. This has also been observed in [23,33,43]. Fig. 8 shows good agreement between

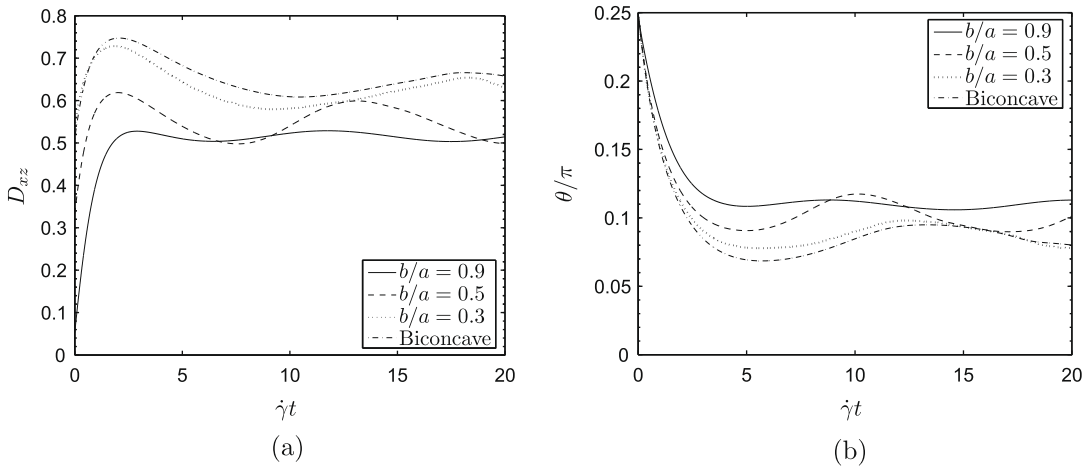

Fig. 13. The time evolutions of (a) the deformation parameter and (b) inclination angle for oblate spheroidal and biconcave capsules with $\lambda = 1$ and $G = 0.2$.

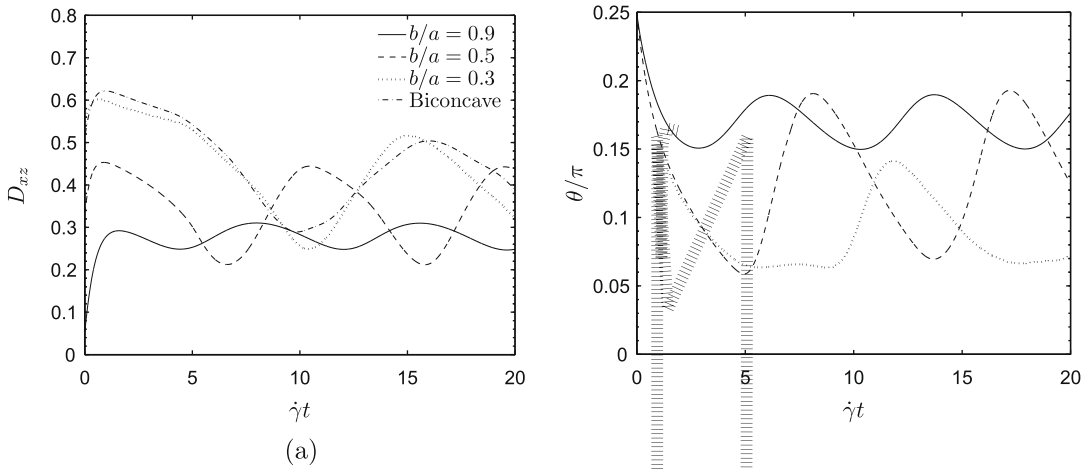

our results and those obtained in [43]. The BEM [33] predicts smaller deformations than the present method and the LBM [43]. And as reported in [23], we can conclude that the deformation parameters obtained by the present thin-shell model agree well with those obtained using the zero-thickness shell description of the membrane behavior. Since the oblate spheroid with $b/a = 0.9$ is a nearly spherical capsule, its deformation trends are similar to those of the spherical capsule. An increase in the shear rate G leads to greater deformation and increased alignment with the undisturbed flow.

Fig. 9 shows the time evolutions of the deformation parameter and the inclination angle for oblate spheroidal capsules with $b/a = 0.9$ and $\lambda = 1$ at a range of smaller dimensionless shear rates G. It can be observed from Figs. 8 and 9 that at large shear rate ($G \geqslant 0.01$), the capsule undergoes periodic oscillations in both the deformation parameter and inclination angle superimposed on the tank-treading motion. This mode of motion has also been observed in both theory [1,26,41] and simulations [18,28,44] and is referred as swinging motion. As G is decreased, the amplitude of the oscillations increases especially noticeable in the inclination angle in Fig. 9(b). As G is decreased further, e.g $G = 0.005$, the capsule's motion has changed from swinging to tumbling mode in which the capsule undergoes continuous rotation. Additional simulations were performed for $\lambda = 10$ to study the effect of viscosity ratio on the deformation and inclination. Fig. 10 suggests that an increase in λ results in lower deformation but amplifies the oscillation. The change in the capsule's motion from tumbling to swinging can be observed from Fig. 10(b) as G is raised.

We also observe a transient dynamics from tumbling to tank-treading as shown in Fig. 11 for the oblate spheroidal capsules with $b/a = 0.9$ and $\lambda = 1$ at $G = 0.0072$ and $G = 0.0074$. To quantify the oscillations in the swinging, tumbling and transient states we follow [18] to define a phase angle as

$$\delta(t) = \alpha(t) - \theta(t) - (\alpha(\mathbf{0}) - \theta(\mathbf{0})), \tag{75}$$

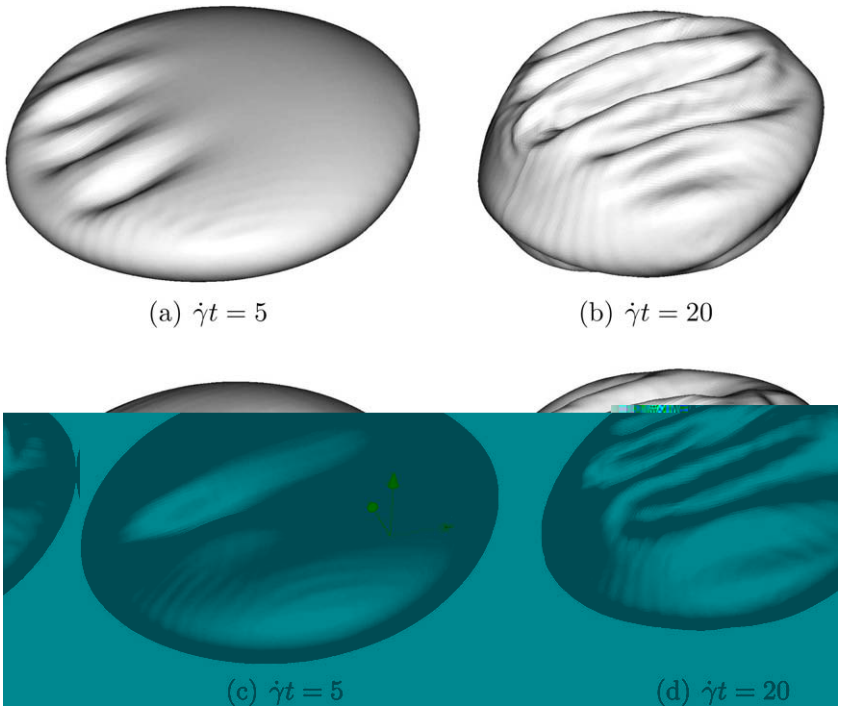

Fig. 15. Shapes of spheroid capsule with $b/a = 0.3$ at (a) $\dot{\gamma}t = 5$, (b) $\dot{\gamma}t = 20$ and biconcave capsule at (c) $\dot{\gamma}t = 5$ and (d) $\dot{\gamma}t = 20$ with $\lambda = 1$ and $G = 0.05$.

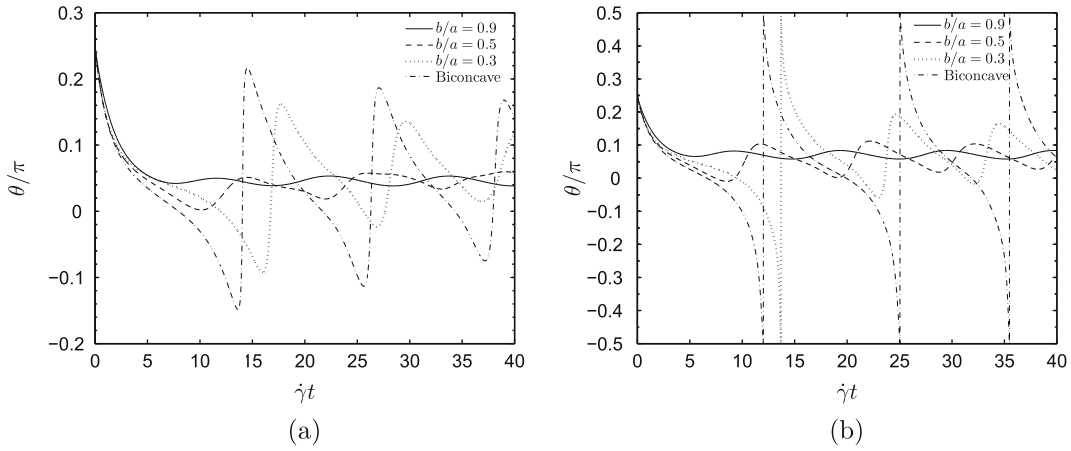

Fig. 16. The time evolutions of the inclination angle for oblate spheroidal and biconcave capsules with $\lambda = 5$ and (a) $G = 0.2$, (b) $G = 0.1$.

where $\alpha(t)$ is the tank-treading angle of a marker point on the membrane compared to the undisturbed flow direction. To make $\delta(t)$ a continuous function of time, we manually subtract π from $\alpha(t)$ or $\theta(t)$ after their values make a half rotation. Fig. 12 shows typical plots of inclination angle θ vs. phase angle δ for oblate spheroidal capsules with $b/a = 0.9$ and $\lambda = 1$ at different states of motion. The arrows indicate the direction of time in the plot. In the swinging motion the inclination angle θ undergoes periodic oscillations while the phase angle δ changes monotonically with time as shown in Fig. 12(a). In the tumbling motion, the inclination angle θ changes monotonically with time while the phase angle δ undergoes periodic oscillations around a stationary value as shown in Fig. 12(b). Fig. 12(c) and (d) shows the behaviors of θ and δ at the transition from a tumbling motion to a swinging motion.

Next, we consider spheroidal capsules with more oblate unstressed shape of aspect ratios $b/a = 0.5$ and 0.3, inclined at the angle $\theta = \pi/4$ with respect to the streamlines of the unperturbed flow. In addition, we consider capsules with unstressed shapes of biconcave disks. The deformation parameter D_{xz} and inclination angle θ are calculated for oblate capsules with $\lambda = 1$ and $G = 0.2$ and are shown in Fig. 13. Fig. 14 shows the evolution of D_{xz} and θ at smaller dimensionless shear rate

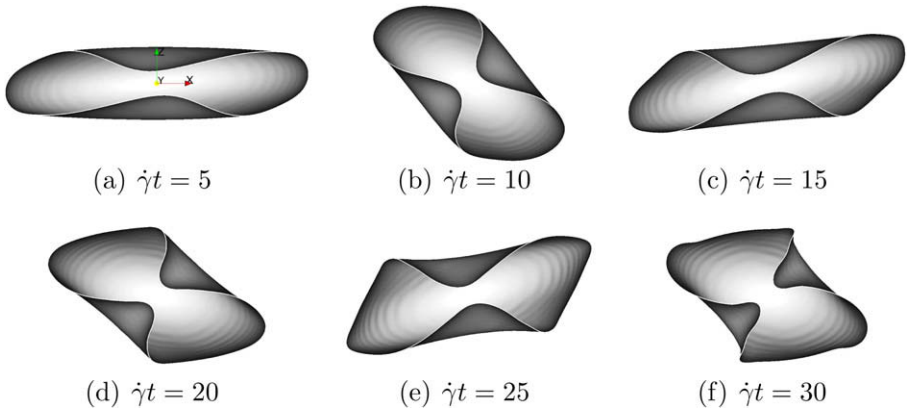

Fig. 17. Shapes of the neo-Hookean biconcave disk with $\lambda = 10$ and $G = 0.2$ during tumbling motion.

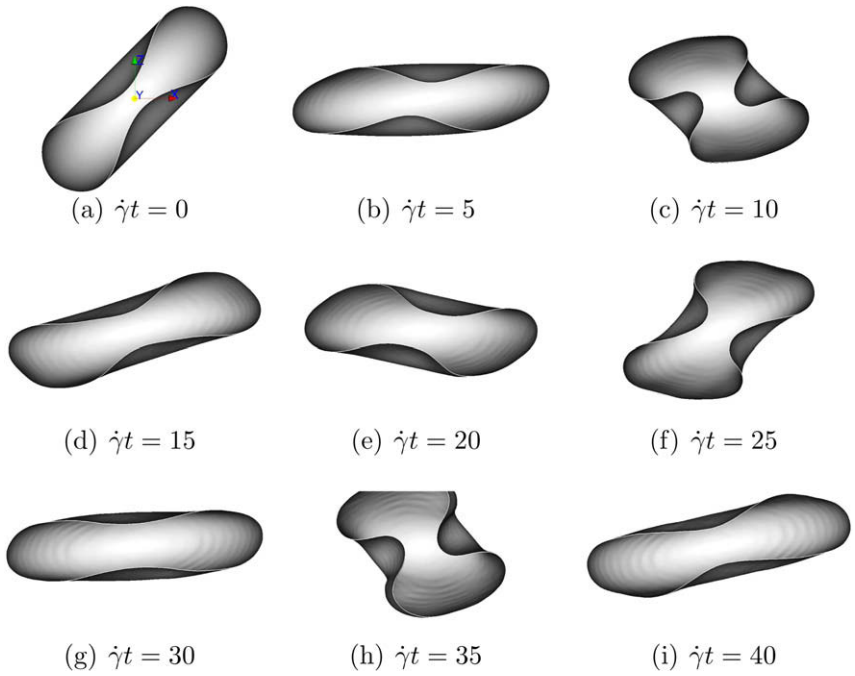

Fig. 18. Shapes of the Skalak biconcave disk with $\lambda = 5$ and $G = 0.2$ during tumbling motion.

$G = 0.05$. In both cases, the capsules rotate around the internal fluid in a tank–treading mode. For the spheroid with $b/a = 0.5$, sustained oscillations in D_{xz} and θ with larger amplitude at smaller G can be observed. Oscillations in D_{xz} and θ are also seen for the spheroidal capsule with $b/a = 0.3$ and the biconcave disk. The behavior of the spheroid with $b/a = 0.3$ is similar to that of the biconcave disk throughout the course of the simulation owing to the similarity in shape and surface area of both capsules. In [33], numerical instabilities due to the grid degradation limited the extent of the simulations for the spheroid with $b/a = 0.3$ and the biconcave disk. With the present thin-shell model, we are able to increase the duration of the simulations further. However, the simulations capture the buckling instabilities at low dimensionless shear rate G due to the compressive stress [21,24] as seen in Fig. 15.

Next, we perform additional simulations for $\lambda = 5$ with $G = 0.2$ and $G = 0.1$. The temporal evolution profiles for the inclination angle are shown in Fig. 16. At $G = 0.2$, we see little change in the character of the response for the spheroid with $b/a = 0.9$ but significant differences in the behavior of the more–oblate spheroids and biconcave disk. The spheroid with $b/a = 0.5$ still undergoes swinging motion but the oscillation amplitudes are larger at $\lambda = 5$ than at $\lambda = 1$. For the $b/a = 0.3$ spheroid and the biconcave disk, the inclination profiles in [33] suggest continuous rotation but there is no clear evidence because of the limited extend of the simulation. In the present study, with longer simulation time we can observe that the inclination angles drop below zero before return to positive angles and the capsules still undergo swing

motion. However, at lower dimensionless shear rate $G = 0.1$ the biconcave disk rotates continuously in the tumbling mode and the transient dynamics from tumbling to swinging can be observed for the $b/a = 0.3$ spheroid as shown in Fig. 16(b). Additional simulations were performed for the biconcave disk with $\lambda = 10$ deforming at $G = 0.2$. The shapes of the biconcave disk at different times are show in Fig. 17. These shapes indicate that the biconcave capsule rotates continuously in the clockwise direction and that with increasing λ the flow triggers the tumbling motion at a larger dimensionless shear rate.

Finally, we perform simulations for the biconcave disk with Skalak's strain energy function at $G = 0.2$ and $\lambda = 5$. The ratio between the area dilation modulus and the shear elastic modulus, c_{11}, is chosen to be 50, which is large enough to maintain the constant area of the biconcave capsule. The simulation results show that the capsule surface area and volume changes are within 0.8% and 0.2%, respectively and the capsule undergoes tumbling motion. Fig. 18 shows the snapshots of the biconcave disk during tumbling motion.

5. Conclusions

In this paper, we have presented a thin-shell model to study the deformations of liquid capsules enclosed by elastic thin shells in the shear flow. The thin-shell model is used in conjunction with the implicit immersed boundary method for the incompressible Navier–Stokes equations which enable us to handle three-dimensional fluid–structure interactions. The present method was validated by studying the inflation of a spherical shell and the deformations of spherical and oblate spheroidal capsules. The problem of the inflation of a sphere tests the accuracy and convergence properties of the thin-shell model under conditions of large membrane deformations. Good agreement between exact and numerical solutions and the general trend towards convergence have been demonstrated in this example. For the spherical capsule in shear flow, computations are performed to reproduce the deformation parameters and inclination angles at different dimensionless shear rates and material properties. Our numerical results show excellent agreement with published theoretical and numerical results. Simulations have also been performed for the oblate spheroidal and biconcave capsules over a wide range of dimensionless shear rates and viscosity ratios with different strain energy functions. Different types of motion such as tank-treading, tumbling and transition from tumbling to tank-treading have been observed for oblate spheroidal capsules depending on the shear rate and viscosity ratio. We have also quantified the oscillations in the tank-treading, tumbling and transient motions by defining the phase angle.

The present method for computing the forces based on the thin-shell model significantly improves our ability to simulate capsules with hyperelastic membranes, enabling us to study large deformations of capsules with different unstressed shapes. The improvements in the numerical method also allow us to overcome numerical instability resulting from the degradation of the grid. The method can be improved further by improving the smoothness of the surface. For the current unstructured mesh, it is not possible to ensure C^1 continuity across finite elements since the finite elements are endowed with purely local polynomial shape functions. To ensure a continuous description of the high-order geometrical quantities such as curvature, one may use subdivision surfaces for generating smooth surfaces. This is a topic of a current investigation.

References

[1] M. Abkarian, M. Faivre, A. Viallat, Swinging of red blood cells under shear flow, Phys. Rev. Lett. 98 (2007) 188302.
[2] Y. Başar, Y. Ding, Finite-element analysis of hyperelastic thin shells with large strains, Comput. Mech. 18 (1996) 200–214.
[3] D. Barthès-Biesel, Motion of spherical microcapsule freely suspended in a linear shear flow, J. Fluid Mech. 100 (1980) 831–853.
[4] D. Barthès-Biesel, J.M. Rallison, The time-dependent deformation of a capsule freely suspended in a linear shear flow, J. Fluid Mech. 113 (1981) 251–267.
[5] D.L. Brown, R. Cortez, M.L. Minion, Accurate projection methods for the incompressible Navier–Stokes equations, J. Comput. Phys. 168 (2001) 464–499.
[6] K.S. Chang, W.L. Olbricht, Experimental studies of the deformation and break-up of a synthetic capsule in steady and unsteady simple shear flow, J. Fluid Mech. 250 (1993) 609–633.
[7] J.M. Charrier, S. Shrivastava, R. Wu, Free and constrained inflation of elastic membranes in relation to thermoforming nonaxisymmetric problems, J. Strain Anal. 24 (1989) 55–74.
[8] F. Cirak, M. Ortizm, Fully C^1-conforming subdivision elements for finite deformation thin-shell analysis, Int. J. Numer. Methods Eng. 51 (2001) 813–833.
[9] F. Cirak, M. Ortiz, P. Schroder, Subdivision surfaces: a new paradigm for thin-shell finite-element analysis, Int. J. Numer. Methods Eng. 47 (2000) 2039–2072.
[10] S.K. Doddi, P. Bagchi, Three-dimensional computational modeling of multiple deformable cells flowing in microvessels, Phys. Rev. E 79 (2009) 046318.
[11] J. Douglas, Alternating direction methods for three space variables, Numer. Math. 4 (1962) 41–63.
[12] R. Eberlein, P. Wriggers, R.L. Taylor, A fully non-linear axisymmetrical quasi-Kirchhoff-type shell element for rubber-like materials, Int. J. Numer. Methods Eng. 36 (1993) 4027–4043.
[13] C.D. Eggleton, A.S. Popel, Large deformation of red blood cell ghosts in a simple shear flow, Phys. Fluids 10 (1998) 1834–1845.
[14] E. Evans, Y.C. Fung, Improved measurements of the erythrocyte geometry, Microvasc. Res. 4 (1972) 335–347.
[15] T.M. Fischer, Shape memory of human red blood cells, Biophys. J. 86 (2004) 3304–3313.
[16] F. Gruttmann, R.L. Taylor, Theory and finite element formulation of rubberlike membrane shells using principal stretches, Int. J. Numer. Methods Eng. 35 (1992) 1111–1126.
[17] A. Hadjidimos, On some high accuracy difference schemes for solving elliptic equations, Numer. Math. 13 (1969) 396–403.
[18] S. Kessler, R. Finken, U. Seifert, Swinging and tumbling of elastic capsules in shear flow, J. Fluid. Mech. 605 (2008) 207–226.
[19] J. Kim, P. Moin, Application of a fractional step method to incompressible Navier–Stokes equations, J. Comput. Phys. 59 (1985) 308–323.
[20] D.A. Knoll, D.E. Keyes, Jacobian-free Newton–Krylov methods: a survey of approaches and applications, J. Comput. Phys 193 (2004) 357–397.
[21] E. Lac, D. Barthès-Biesel, N.A. Pelekasis, J. Tsamopoulos, Spherical capsules in three-dimensional unbounded Stokes flows: effect of the membrane constitutive law and onset of buckling, J. Fluid Mech. 516 (2004) 303–334.
[22] D.V. Le, B.C. Khoo, K.M. Lim, An implicit-forcing immersed boundary method for simulating viscous flows in irregular domains, Comput. Methods Appl. Mech. Eng. 197 (2008) 2119–2130.

[23] D.V. Le, J. White, J. Peraire, K.M. Lim, B.C. Khoo, An implicit immersed boundary method for three-dimensional fluid-membrane interactions, J. Comput. Phys. 228 (2009) 8427–8445.
[24] X. Li, K. Sarkar, Front tracking simulation of deformation and buckling instability of a liquid capsule enclosed by an elastic membrane, J. Comput. Phys. 227 (2008) 4998–5018.
[25] J.E. Marsden, T.J. R Hughes, Mathematical Foundations of Elasticity, Prentice-Hall, Englewood Cliffs, NJ, 1983.
[26] C. Misbah, Vacillating breathing and tumbling of vesicles under shear flow, Phys. Rev. Lett. 96 (2006) 028104.
[27] A. Needleman, Inflation of spherical rubber balloons, Int. J. Solids Struct. 13 (1977) 409–421.
[28] H. Noguchi, G. Gompper, Swinging and tumbling of fluid vesicles in shear flow, Phys. Rev. Lett. 98 (2007) 128103.
[29] R.W. Ogden, Non-Linear Elastic Deformations, Ellis Horwood, Chichester, UK, 1984.
[30] C.S. Peskin, The immersed boundary method, Acta Numer. 11 (2) (2002) 479–517.
[31] C. Pozrikidis, Numerical Computation in Science and Engineering, Oxford University Press, 1998.
[32] C. Pozrikidis, Effect of membrane bending stiffness on the deformation of capsules in simple shear flow, J. Fluid Mech. 440 (2001) 269–291.
[33] S. Ramanujan, C. Pozrikidis, Deformation of liquid capsules enclosed by elastic membrane in simple shear flow: large deformations and the effect of fluid viscosities, J. Fluid Mech. 361 (1998) 117–143.
[34] A.M. Roma, C.S. Peskin, M.J. Berger, An adaptive version of the immersed boundary method, J. Comput. Phys. 153 (1999) 509–534.
[35] H. Schmid-Schönbein, R.E. Wells, Fluid drop like transition of erythrocytes under shear, Science 165 (1969) 288–291.
[36] U. Schumann, R.A. Sweet, A direct method for the solution of Poisson's equation with Neumann boundary conditions on a staggered grid of arbitrary size, J. Comput. Phys. 20 (1976) 171–182.
[37] S. Shrivastava, J. Tang, Large deformation finite element analysis of non-linear viscoelastic membranes with reference to thermoforming, J. Strain Anal. 28 (1993) 31–51.
[38] J.C. Simo, D.D. Fox, On a stress resultant geometrically exact shell model. Part I: Formulation and optimal parametrization, Comput. Methods Appl. Mech. Eng. 72 (1989) 267–304.
[39] J.C. Simo, D.D. Fox, On a stress resultant geometrically exact shell model. Part IV: Variable thickness shells with through-the-thickness stretching, Comput. Methods Appl. Mech. Eng. 81 (1990) 91–126.
[40] R. Skalak, A. Tozeren, R.P. Zarda, S. Chien, Strain energy function of red blood cell membranes, Biophys. J. 13 (1973) 245–264.
[41] J.M. Skotheim, T.W. Secomb, Red blood cells and other nonspherical capsules in shear flow: oscillatory dynamics and the tank-treading-to-tumbling transition, Phys. Rev. Lett. 98 (2007) 078301.
[42] J. Stam, Fast evaluation of loop triangular subdivision surfaces at arbitrary parameter values, in: Computer Graphics (SIGGRAPH'98 Proceedings, CD-ROM supplement), 1998.
[43] Y. Sui, Y.T. Chew, P. Roy, H.T. Low, A hybrid method to study flow-induced deformation of three-dimensional capsules, J. Comput. Phys. 227 (2008) 6351–6371.
[44] Y. Sui, H.T. Low, Y.T. Chew, P. Roy, Tank-treading, swinging, and tumbling of liquid-filled elastic capsules in shear flow, Phys. Rev. E 77 (2008) 016310.
[45] G. Tryggvason, B. Bunner, A. Esmaeeli, D. Juric, N. Al-Rawahi, W. Tauber, J. Han, S. Nas, Y.-J. Janz, A front-tracking method for the computations of multiphase flow, J. Comput. Phys. 169 (2001) 708–759.
[46] S.O. Unverdi, G. Tryggvason, A front-tracking method for viscous, incompressible flows, multi-fluid flows, J. Comput. Phys. 100 (1992) 25–37.
[47] A. Walter, H. Rehage, H. Leonhard, Shear-induced deformation of polyamid microcapsules, Colloid Polymer Sci. 278 (2000) 169–175.
[48] A. Walter, H. Rehage, H. Leonhard, Shear induced deformation of microcapsules: shape oscillations and membrane folding, Colloids Surf. A: Physicochem. Eng. Aspects 183–185 (2001) 123–132.